International Journal of Mechanical Engineering and Applications
2024, Vol. 12, No. 4, pp. 81-99
https://doi.org/10.11648/j.ijmea.20241204.11

Research Article

Design and Modeling of a Long Range Motion Compliant Nanopositioning Stage Driven by a Normal Stressed Electromagnetic Actuator

Chido Celine Chogugudza*, Yan-Ning Fang, Zi-Hui Zhu

Department of Mechanical Engineering, Nanjing University of Science and Technology, Nanjing, China

Abstract

Compliant nanopositioning stages with built-in ultra-precision actuators are frequently integrated into production and analysis instruments comprising ultra-high precision motion generation systems. These stages are essential nanotechnology and advanced material analysis components, providing precise positioning capabilities for various applications. However, in the practical engineering field, there is a lack of compliant nanopositioning stages that can achieve a long-range motion while maintaining accuracy, reliability, and compact size, which is the inspiration for this research. This paper investigates the design, modeling, and experimental testing of a long-range motion-compliant nanopositioning stage driven by a normal stressed electromagnetic actuator (NSEA). The nanopositioning stage components' structural framework and working principle, including NSEA, bridge type distributed compliant (BTDC) mechanism, and the guiding mechanism, are fully examined to derive an analytical model. The analytical model is utilized in the sections that follow. Factors affecting the stroke and natural frequency of the nanopositioning stage are also illustrated. The optimization process of the nanopositioning stage is conducted in pursuit of a high-precision stage by specifically looking into the electromagnetic, BTDC mechanism, and guiding mechanism parameters. This optimization procedure also takes into account various design constraints, including stiffness, saturation flux density, and stress. Furthermore, the finite element analysis is used to verify the analytical model, and the results are discussed. The prototype is fabricated with reference to the analytical and finite element analysis results, and the experimental tests are conducted, including motion and natural frequency tests. In addition, a control system, which adopts both a proportional-integral-derivative controller and a damping controller, is designed to create a closed-loop system. Finally, the tracking performance of the stage was investigated, and a very minimal tracking error was observed. Overall, the comprehensive models and experimental tests proved the stage to be a good model which achieved the objective of the research.

Keywords

Nanopositioning Stage, Normal Stressed Electromagnetic Actuator, Bridge-Type Distributed Compliant Mechanism, Long Range Motion

*Corresponding author:celinechido@njust.edu.cn (Chido Celine Chogugudza)

Received: 19 May 2024; **Accepted:** 30 May 2024; **Published:** 6 September 2024

1. Introduction

Many nanotechnology applications and advanced material analysis involve compliant nanopositioning stages, which are frequently built into manufacturing and analysis tools, including lithographic mechanisms, cell manipulation systems, and optical microscopes [1, 2]. Compliant mechanisms have the ability to boost performance, including high precision due to reduced wear repetitive motion, eliminated backlash [3], and are beneficial in weight-sensitive applications. In order to generate actuation force, compliant nanopositioning stages often employ electromagnetic actuators and smart material-based actuators [4]. Piezoelectric actuator (PEA) is one of the most thoroughly investigated actuators in practical engineering due to its favorable rapid response, high precision, compact size, and high stiffness. However, PEA produces relatively small displacement, limiting its application in long working-range operations [5, 6]. As a result, attention has recently been drawn to the normal stressed electromagnetic actuator (NSEA), which achieves more acceleration than a shear-stressed actuator and functions within a larger frequency range than the PEA. The NSEA also has lower heat dissipation due to its increased force density in the air gap normal direction [7]. Despite its positive traits, a displacement amplification mechanism is required to recognize the potential of the NSEA fully.

Compliant mechanisms that achieve output motion through the deformation of flexible components possess various positive traits over conventional movable joints, including a more efficient assembly period [8]. The displacement amplifiers are categorized into lever-type, flexi-tensional type [9], and Scott Russell mechanism by Taguchi method [10]. Flexi-tensional compliant mechanisms are highly praised for their compact size and higher stiffness. They have evolved from early mechanisms such as rainbow type [11] to the second generation mechanisms, including the bridge type mechanism, followed by various derivative structures like the nested cellular mechanism [12]. In contrast to the mechanisms mentioned above, the bridge type mechanism remains the foundation and basis of most complex compliant mechanisms while showing beneficial traits such as a large amplification ratio and high resonant. In previous literature, the bridge-type lumped compliant structures that use the notch flexure hinges have been used extensively [13, 14]; however, the presence of rigid bodies on the four flexure hinges of the bridge has a significant adverse effect on the resonant frequency of the mechanism [5, 15]. In this research, the bridge type distributed compliant (BTDC) mechanism is adopted as the displacement amplifier because it uses four beam flexure hinges that exclude rigid bodies in between. The bending response of the beam flexure under the NSEA actuation enables an adequate distribution of the stresses in the BTDC mechanism, ensuring a longer life span and greater performance and efficiency than conventional mechanical amplifiers in dynamic applications. The drawback of the BTDC mechanism lies in the comparatively low lateral stiffness [3]. When the output end connector places a significant lateral load on the amplifier, the output body connected to the end connector is prone to damage due to the limited lateral stiffness of the amplifier, which will have a low tolerance for this external load. To overcome this, multiple bridges should be adopted; hence, a BTDC mechanism composed of a double bridge should be fabricated.

Many researchers have shed some light on optimizing the NSEA structure and bridge type mechanism, respectively. According to [16], accuracy is an ongoing concern in optic manufacturing, and both static and dynamic analyses are crucial to minimize errors and enhance structure quality. Jin and Wang [17] clearly illustrated the need for improvement and optimization of the electromagnetic actuators to validate their performance since the high magnetoresistance of the working air gap limits them. In addition, the efficiency of the magnetic circuit and the output stability of the actuator were improved. Chen et al. [18] also presented a design methodology that facilitated the parameter selection of an NSEA-driven nanopositioning stage to obtain the required stroke and natural frequency whilst incorporating a flexure mechanism in the design. Based on Castigliano's second theorem and strain energy, Lobontiu and Garcia deduced a complex analytical method for displacement and stiffness calculations for flexure-based compliant mechanisms [19]. Design techniques, however, require simple analytical models that are sufficiently precise to anticipate the mechanism's performance and further identify its architectural characteristics per the performance requirements. Based on the elastic beam theory, Liu [20] presented a theoretical model that predicts displacement amplification ratio and established an analysis for bridge-type amplification mechanism that takes into account the effects of external loads and provides a new viewpoint into the manufacturing of flexure-based nano stages in the industry. Nonetheless, the mechanical properties of the BTDC mechanism and NSEA have still not been fully discovered. With the contemporary need to manipulate the NSEA-driven structures to produce a large stroke in practical engineering, this research realizes the simultaneous potential of the NSEA and bridge-type structure to produce a greater stroke and travel range motion.

The remainder of this paper is structured as follows: Section 2 presents the design layout and working principle of the nanopositioning stage components, including the NSEA, BTDC mechanism, and the guiding mechanism. The factors influencing stroke and natural frequency are also displayed. In section 3, the stage parameters are optimized, and the results are discussed. The design constraints impacting the optimization process are discussed, and the analytical model results are verified using FEA simulation. In section 4, the experimental procedure is done using open and closed-loop testing. A control system is designed and tracking error derived. Lastly, the main conclusion is drawn in section 5.

2. Static Modeling of the Nanopositioning Stage

2.1. Structure Configuration of the Stage

The nanopositioning stage displayed in Figure 1 comprises two normal stressed electromagnetic actuators (NSEAs), a bridge-type distributed compliant (BTDC) mechanism, and the guiding mechanism encased in one bottom cover and two top covers. Each set of the NSEA consists of the outer stator that is subsequently mounted on the bottom cover and is wound with coil windings. The middle stator is also attached to the bottom cover, which positions the armatures in the center. Fastened to their corresponding covers, the PMs are also attached to PM stators.

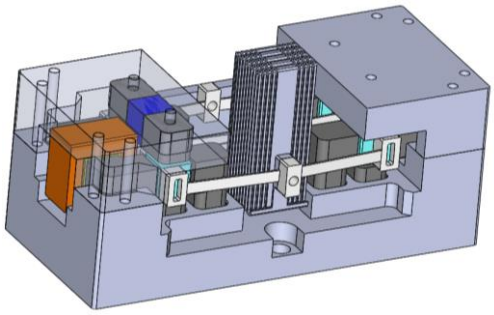

Figure 1. *Nanopositioning stage.*

The armatures within the NSEA also serve as the BTDC mechanism's input bodies, enabling a small-sized nanopositioning stage. These input bodies are coupled to flexure hinges, forming a bridge. A guiding mechanism is attached to the output end of the BTDC mechanism whilst the other end is secured to the bottom cover. The guiding mechanism, NSEA, and BTDC mechanism collectively constitute the nanopositioning stage and operate in unison to produce the final motion. The operation of the nanopositioning stage is further demonstrated by a detailed explanation of its component designs and working principles.

2.2. Design Layout and Working Principle of NSEA

Despite minimal research, NSEA has the ability to perform large force density in a relatively long-range motion. The 3D layout of the NSEA is clearly shown in Figure 2. In essence, the effective working air gap between the armature and stator limits the travel range of NSEA. In order to produce linear motions for the NSEA, stators, and armatures are produced independently and assembled together, necessitating highly precise manufacturing accuracy to maintain the desired air gaps. Both the armatures and the stators are made of soft magnetic material. Unlike traditional normal stressed actuators [21], the entire armature region contributes to force generation, reducing inertial load and heat dissipation caused by eddy currents and hysteresis. Suspended both above and below the two armatures whilst bound by stators on the north and south sides, the two PMs are employed to produce DC biasing flux B_D. The excitation coil windings are serially connected to the outer stator to generate an AC flux B_A for armature actuation. The total excitation coil windings NI will act as the magnetomotive force MMF, which is the magnetic pressure that will set up magnetic flux in the circuit, and the maMMF and the reluctance of the magnetic circuit then determine the magnitude of the flux density. The tracking performance for the NSEA in high-frequency operation is adversely affected due to the nonlinear behavior of the actuating force, which increases the difficulty of control and plant complexity [7]. Despite the contrary, nonlinearity is eliminated by utilizing biasing flux from the permanent magnets in the actuating structure. A linear relationship between the actuation force and the driving current is achieved to attain a high-precision motion control.

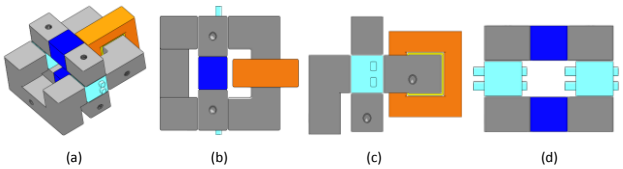

Figure 2. *(a) 3D Layout of NSEA; (b) NSEA top view; (c) NSEA front view; (d) NSEA middle part.*

On the left and right side of each armature consists of air gaps that are designated as $g_0 + x$ and $g_0 - x$ respectively. When the armature is centered, the air gap is denoted as g_0 and the armature displacement x is taken as negative for the movement to the left and positive for movement to the right. After the superpositioning of the biasing flux and excitation flux, the flux density on one side of the armature becomes stronger than the other side; as a result, a noncontact attractive force is generated between the armature and the stator, and the x−axis translational motion is realized.

2.2.1. Biasing Flux Analysis

By taking into account the XY-plane of the NSEA structure in Figure 3(a), the DC flux densities B_{D1} and B_{D2}, are achieved by considering the armature movement x from the center of the two working air gaps of each armature, respectively. Despite being positive when pointed externally at the armature, B_{D1} and B_{D2} have dissimilar reference directions. Due to the suspension of the PMs in the YZ plane, the biasing flux will migrate from the PMs and simultaneously enter through the top and bottom parts of the armature, as illustrated in Figure 3(b).

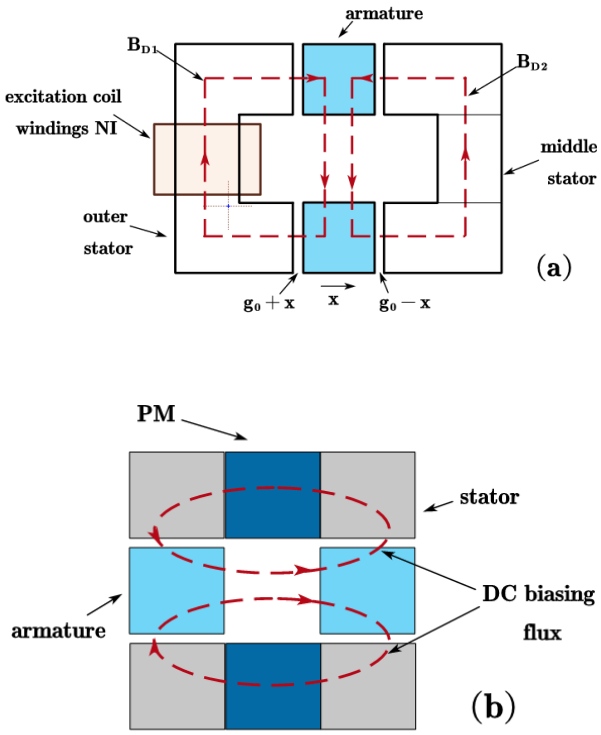

Figure 3. (a) XY-plane of NSEA structure; (b) YZ-plane of NSEA structure.

Upon entering the armature, the biasing flux splits and exists through the right and left air gap. The total flux flowing from the PMs into respective armatures is labeled as Φ_{PM} and S_{wp} is the stator pole face area at each working air gap. Based on the Gaussian Law and analyzing the area where biasing flux enters each armature, the following is derived:

$$\Phi_{PM} - (B_{D1} + B_{D2})S_{wp} = 0 \tag{1}$$

With the magnetic permeability μ predicted as infinite inside the stators and armatures and the current from excitation coil windings set as zero, while taking into consideration the above equation, Ampere's Law is applied to yield:

$$\oint_c \vec{H} \vec{dl} = 0, \tag{2}$$

$$B_{D1} = \frac{g_0+x}{g_0} B_D, B_{D2} = \frac{g_0-x}{g_0} B_D \tag{3}$$

The average DC bias flux from the PM into the pole surface of the stator is denoted as B_D which can be expressed as follows:

$$B_D = \frac{\alpha_{IF} B_r S_{PM}}{2S_{ST}}, \tag{4}$$

where $B_r = \phi_{PM}/S_{PM}$ is the remanence of PM. S_{PM} and S_{ST} are the pole surface area of the PM and stator, respectively.

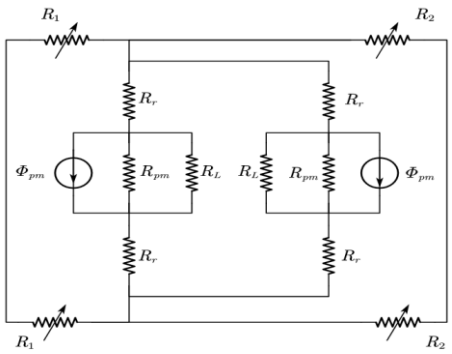

Figure 4. Equivalent DC magnetic circuit model in NSEA.

Due to the symmetry of the set of the compliant mechanism, only the equivalent DC magnetic circuit model in one of the NSEAs is needed for analysis. In the magnetic circuit, two PMs with internal-reluctance R_{PM} are the source of the continuous magnetic flux, and ϕ_{PM} represents the total flux passing through each PM when its internal magnetic field is zero. Each of the two PMs has a leakage path that is referred to as reluctance. R_L, and in the vertical direction between every armature and PM, there is also a reluctance labeled R_r. In the x-plane of the NSEA structure, there are air gaps in the left and right side of the two armatures, and on each armature, there are labelled as variable reluctances. R_1 and R_2 respectively. Based on the electromagnetic model, the reluctances above are mathematically expressed as:

$$\begin{cases} R_1 = \frac{g_0 - x}{\mu_0 S_{ST}} \\ R_2 = \frac{g_0 + x}{\mu_0 S_{ST}} \\ R_{PM} = \frac{L_{PM}}{\mu_0 S_{PM}} \\ R_r = \frac{L_{AP}}{\mu_0 S_{PM}} \end{cases} \tag{5}$$

where R_{PM} and L_{PM} represent the internal reluctance and length of the PM, respectively. L_{AP} is the length of the air gap between the PM and armature. By identifying the flux from PM into the armature as Φ and the total flux flowing out of the PM as Φ_T, the reluctance ratio is expressed as:

$$\frac{\phi}{\phi_T} = \frac{2R_L}{2(R_1//R_2)+4R_r+2R_L} \tag{6}$$

By further demonstrating that R_r is significantly larger than $R_1//R_2$ whose maximum value is reached when the armature is centered and based on this armature position, the following is obtained:

$$\frac{R_1//R_2}{R_r} = \frac{g_0 S_{PM}}{2S_{ST}L_{AP}} \tag{7}$$

The combination of Equations (6) and (7) yields R_L which is expressed as a fraction of R_r. In light of this, $R_1//R_2$ and its fluctuation with location x are insignificant in comparison

to R_L andR_r. Following the application of circuit principles to the equivalent DC magnetic model in NSEA, $\bar{\phi}$ is stated as:

$$\bar{\phi} = \alpha_{IF}\phi_{PM} \tag{8}$$

The leakage factor α_{IF} from the above equation (8) is further illustrated as:

$$\alpha_{IF} = \frac{2(R_{PM}//R_L)}{2(R_{PM}//R_L)+4R_r+2(R_1//R_2)} \tag{9}$$

2.2.2. AC Flux Analysis

The AC flux densities B_{A1} and B_{A2} are produced by the total excitation coil windings NI. It is assumed that there is only one closed circuit linked to AC flux and the two permanent magnets have been taken out when the AC flux generation is being examined. Given that the two armature polar surfaces have equal effective areas, regardless of the armature motion x, the resultant AC flux travelling through each of the surfaces may be similar [18]. Under the assumption that the soft magnetic material used in fabricating armatures and stators has infinite permeability and μ_0 denotes the vacuum permeability, the total AC flux can be expressed as follows:

$$B_{A1} = B_{A2} = B_A = \frac{\mu_0 NI}{2g_0} \tag{10}$$

This demonstrates categorically that AC flux density is independent of the armature displacement, and the linear relationship between the AC flux density and the excitation current exists. The induced actuation force imposed on the polar surface of the armature resulting from the different flux densities inside the left and right air gaps is obtained using Maxwell's stress tensor theory. The actuation force on one armature can be expressed by:

$$\begin{cases} F_1 = \frac{S_{ST}}{2\mu_0}[(B_A + B_{D1})^2], \\ F_2 = \frac{S_{ST}}{2\mu_0}[(B_A - B_{D2})^2], \\ F = F_1 - F_2 \end{cases} \tag{11}$$

$$F = \left\{\frac{S_{ST}}{2\mu_0}[(B_A + B_{D1})^2 - (B_A - B_{D2})^2]\right\}$$

$$F = \frac{S_{ST}}{\mu_0}\left(\frac{\mu_0 B_D}{g_0}NI + \frac{2{B_D}^2}{g_0}x\right)$$

$$F = K_I I + K_x x \tag{12}$$

Considering this calculation, it foretells that the induced actuating force is a linear function of both the armature displacement x and the excitation current; and the constant coefficients of both. K_I and K_x are influenced by the material and armature dimensional characteristics. The part $K_x x$ represents an additional flux force generated when the armature departs from the centered position while the $K_I I$ part denotes the anticipated actuation force produced by excitation coil windings. Since there are two armatures in this NSEA structure, the total directional actuation force is twice that generated by one armature.

2.3. Design Layout and Working Principle of BTDC Mechanism

The BTDC mechanism, with single ramp shown in Figure 5 is composed of a fixed body located at the bottom, four input bodies, eight flexure hinges and two output bodies located at the center and top of the bridge in the y-axis direction. This BTDC mechanism is an improved version of the classical bridge mechanism.

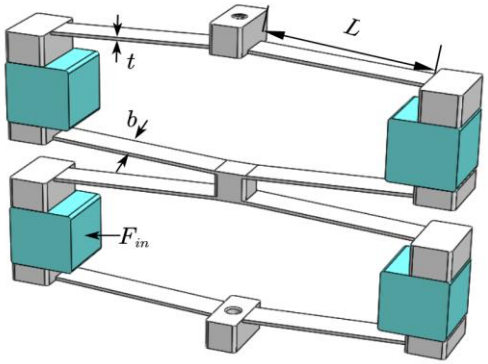

Figure 5. *Bridge type distributed compliant mechanism.*

The actuation force produced by the NSEA triggers the movement of the armatures acting as input bodies along the x-axis direction and due to the position of the flexure hinges whilst linked to the input bodies will cause the motion of the two output bodies in the y-axis direction. Due to the full flexure of this bridge-type mechanism, the overall displacement is primarily attributable to the bending deformations of the entire hinge and along the transverse direction exists the actuating force that creates an angle with the flexure hinge [9]. The schematic diagram of a single flexure hinge of the bridge is shown in Figure 6(a).

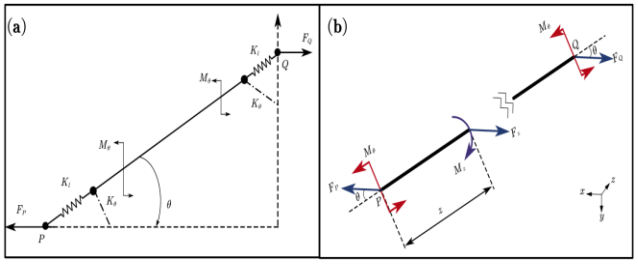

Figure 6. *(a) Mechanics of a flexure hinge; (b) Free body diagram of a flexure hinge.*

2.3.1. Force Analysis of BTDC Mechanism

Due to symmetry, only one of the hinges is mathematically analyzed, and the input and output ends are considered rigid parts after considering their high stiffness [22]. Figure 5 clearly shows the length and thickness of the flexure hinge L and t, respectively, and also the angle between the horizontal line and the flexure hinge baseline θ as the structural parameters of the BTDC mechanism. As in previous literature [23, 24], the internal moments caused by the two hinges are assumed to be identical. To guarantee that the angles of deflection at the two points of connection PQ remain zero, a supplementary moment M_θ is applied. The following relationships can be established by taking into account the moment equilibrium and the force equilibrium along the x-axis:

$$F_P = F_Q = F = \frac{F_{in}}{2} \tag{13}$$

$$M_\theta = \frac{FLsin\theta}{2} = K_\theta \Delta\theta \tag{14}$$

A single flexure hinge is considered to possess two types of stiffness including rotational stiffness K_θ and translational stiffness K_l. Parameters $\Delta\theta$ and Δl represent the angle of rotation and axial tensile displacement, respectively. Based on Hooke's Law and in view of the force status in Figure 6(a), the following relationship is obtained:

$$F_L = Fcos\theta = K_l \Delta l \tag{15}$$

In accordance with the energy conservation principle, the work performed by the force from the NSEA is converted into tensile deformation energy and bending potential energy. Variables including a moment in the elastic beam $M(z)$, Young's modulus E, area A, input displacement Δx, axial tension $F_L(z)$ and moment of inertia of the corresponding axial cross-section I are taken into consideration to derive the resulting equation as follows:

$$\frac{1}{2}F\Delta x = \frac{F^2 cos^2\theta}{2EA}\int_0^L dz + \frac{1}{2EI}\int_0^L M^2(z)\,dz \tag{16}$$

With reference to Figure 6(b) the moment in the elastic beam at the inner part of the flexure hinge at point z can be modeled on how it evolves along the neutral axis as follows:

$$M(z) = M_\theta - Fzsin\theta = Fsin\theta\left(\frac{L}{2} - z\right) \tag{17}$$

The strain energy produced by bending deformation in the mechanism can be obtained as:

$$\frac{1}{2EI}\int_0^L M^2(z)\,dz = \frac{1}{2EI}\int_0^L \left(\frac{FLsin\theta}{2} - Fzsin\theta\right)^2 dz$$

$$= \frac{L^2F^2sin^2\theta}{24K_\theta} \tag{18}$$

The output displacement of the BTDC mechanism in the y-axis direction is derived in simple terms as:

$$\Delta y = Lcos\theta\Delta\theta \tag{19}$$

The correlation between the input displacement and the input force of the structure is established by substituting equation (18) into equation (16). The output displacement is further determined by substituting equation (14) into equation (19). The two resultant equations of input displacement and output displacement are respectively expressed as:

$$\begin{bmatrix}\Delta x\\ \Delta y\end{bmatrix} = F_{in} * \begin{bmatrix}\left(\frac{L^2sin^2\theta}{12K_\theta} + \frac{cos^2\theta}{K_l}\right)\\ \left(\frac{L^2cos\theta sin\theta}{4K_\theta}\right)\end{bmatrix} \tag{20}$$

The relationship between the input and output displacement is further modeled into an amplification ratio as follows:

$$R_{amp} = \frac{\Delta y}{\Delta x} = \frac{3cot\theta}{Pcot^2\theta + 1}, P = \frac{12K_\theta}{K_l L^2} \tag{21}$$

From equation (21), the amplification ratio is dependent on angleθ, length of flexure hinge, and translational and rotational stiffness of the mechanism. Given the input displacement and input force, the input stiffness is determined by the following:

$$K_{in} = \frac{F_{in}}{\Delta x} = \frac{F_{in}}{\left(\frac{L^2sin^2\theta}{12K_\theta} + \frac{cos^2\theta}{K_l}\right) * F_{in}} \tag{22}$$

2.3.2. Stroke Length Analysis

Since this mechanism incorporates the right-angled hinge to enhance the input displacement, the hinge is considered to be a 6 degree of freedom spring element. A series of flexure beams and flexure hinges that join the linked nodes p and q make up the bridge structure. According to [25, 26], the compliance matrix C_{pq} derived from beam theory, force F_{pq} and displacement u_{pq} of either of the flexure element can be expressed as:

$$u_{pq} = C_{pq}F_{pq} : K_{pq} = C_{pq}{}^{-1}, where \begin{cases} F_{pq} = \left[F_x{}^p\ F_y{}^p\ M_z{}^p\ F_x{}^q\ F_y{}^q\ M_z{}^q\right]^T \\ u_{pq} = \left[u_x{}^p\ u_y{}^p\ \theta_z{}^p\ u_x{}^q\ u_y{}^q\ \theta_z{}^q\right]^T \end{cases} \tag{23}$$

From equation (23) it can be deduced that stiffness matrix K_{pq} and the compliance matrix are both symmetrical, regular, and inverse matrices of each other. Considering that $A = b \times t$ as the cross-section area, the stiffness matrices of both the flexure hinge and flexure beam in the local coordinate can individually be expressed as:

$$K_{pq} = \begin{bmatrix} \frac{EA}{L} & 0 & 0 & -\frac{EA}{L} & 0 & 0 \\ 0 & \frac{12EI}{L^3} & \frac{6EI}{L^2} & 0 & -\frac{12EI}{L^3} & \frac{6EI}{L^2} \\ 0 & \frac{6EI}{L^3} & \frac{4EI}{L} & 0 & -\frac{6EI}{L^2} & \frac{2EI}{L} \\ -\frac{EA}{L} & 0 & 0 & \frac{EA}{L} & 0 & 0 \\ 0 & -\frac{12EI}{L^3} & -\frac{6EI}{L^2} & 0 & \frac{12EI}{L^3} & -\frac{6EI}{L^2} \\ 0 & \frac{6EI}{L^2} & \frac{2EI}{L} & 0 & -\frac{6EI}{L^2} & \frac{4EI}{L} \end{bmatrix} \quad (24)$$

Only the planar stiffness needs to be considered for a bridge-type mechanism [27]. So K_l and K_θ is derived from the matrix in equation (24) as follows:

$$K_l = \frac{Ebt}{L}, K_\theta = \frac{Ebt^3}{12L} \quad (25)$$

Stiffness matrix of the flexure element should be transformed into the global coordinate matrix by including a rotational transformation matrix. The counter-clockwise rotation angle θ of the local coordinate of the element with respect to the global coordinate is utilized to establish the rotational transformation matrix as follows:

$$R_{pq} = \begin{bmatrix} cos\theta & sin\theta & 0 & 0 & 0 & 0 \\ -sin\theta & cos\theta & 0 & 0 & 0 & 0 \\ 0 & 0 & 1 & 0 & 0 & 0 \\ 0 & 0 & 0 & cos\theta & sin\theta & 0 \\ 0 & 0 & 0 & -sin\theta & cos\theta & 0 \\ 0 & 0 & 0 & 0 & 0 & 1 \end{bmatrix} \quad (26)$$

Then the elemental stiffness matrix in the global coordinate is given as:

$$K_T^{pq} = {R_{pq}}^T K_{pq} R_{pq} \quad (27)$$

An integral stiffness matrix K_{tot} is developed for the whole BTDC mechanism in accordance with the connection relations depicted in Figure 7, then the motion equation is stated based on the generalized Hooke's law as follows:

$$F = K_{tot} u : \begin{cases} F = [F^1 \dots F^p \dots F^n]^T \\ F^p = [{F_x}^p \, {F_y}^p \, {M_z}^p]^T \\ u = [u^1 \dots u^p \dots u^n]^T \\ u^p = [{u_x}^p \, {u_y}^p \, {\theta_z}^p]^T \end{cases} \quad (28)$$

The overall amount of assigned nodal points for the given bridge structure is 7, and p equates to the integral of 1 up to n. The second nodal point is designated as the fixed location by considering the boundary limitations. Every column and row pertinent to the fixed nodal point is eliminated in order to eradicate singularity. As a result, a displacement vector $\bar{u}$, force vector $\bar{F}$ and stiffness matrix $\overline{K_{tot}}$ are acquired, and the displacement of each unfixed nodal point is determined using the equation as follows:

$$\bar{u} = \bar{F} / \overline{K_{tot}} \quad (29)$$

There are two output nodal points, 4 and 7, and the total accumulative induced actuation force. F_y along the y-axis will act on the outward output nodal point 7, and the variable u_y^{out} and u_y^7 is the displacement of the output nodal point along the y−axis. The stiffness of the BTDC mechanism along the y−axis whilst negating the elastic deformation of the flexure beam attached to the output nodal point is then determined as:

$$K_{tot} = \frac{F_y}{u_y^{out}} = \frac{2F}{u_y^7} \quad (30)$$

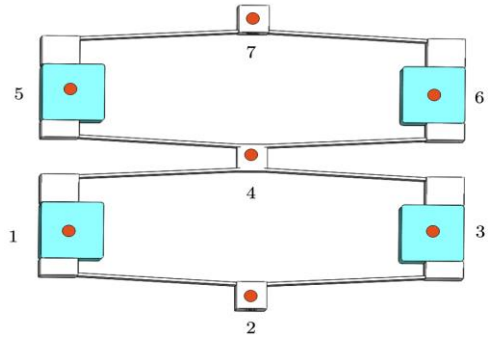

Figure 7. *Nodal point connecting relationship of the BTDC mechanism.*

To realize the full potential of the BTDC mechanism working stroke in the y-axis direction, the actuation force is analyzed further without merely restricting the force calculation to when the armature is centered, but the part of the actuation force that accounts for the displacement of the armature in equation (12) is evaluated in detail. As the K_x increases in size, the calculation based on the armature being centered becomes incorrect due to the fact that F_x which contributes the armature movement in the x-axis becomes significantly. Although considering armature being centered simplifies analytical calculation, it introduces inaccuracy. Following the consideration of displacement as $x = u_x^{in} = u_x^1 = u_x^3 = u_x^5 = u_x^6$, the overall force exerted on the bridge mechanism is determined as:

$$F_a = 4F_{in} = 4(K_I I + K_x u_x^1),$$

$$where \;\; F_{in} = K_{tot} u_x^1 \quad (31)$$

Assuming that input displacement x is at the maximum position, the relation between the excitation current and displacement is further derived as:

$$K_{tot} x = K_I I + K_x x$$

$$x = \frac{K_I I}{K_{tot} - K_x} \tag{32}$$

The stroke length at the nodal point 4 in y-axis direction is then expressed as:

$$\Delta y_{s4} = 2\left(\frac{F_a}{K_{tot}} R_{amp} X_{max}\right)$$

$$\Delta y_{s4} = 2\left(\frac{F_a}{K_{tot}} * R_{amp} * \left(\frac{K_I I}{K_{tot} - K_x}\right)\right) \tag{33}$$

In accordance with the BTDC mechanism working principle, the stroke length at nodal point 7, Δy_{s7} is twice as long as that at nodal point 4. The fact that K_I, K_x and K_{tot} are constants illustrate that both the actuation force and output displacement are directly related to the excitation current I.

2.3.3. Dynamic Analysis of the BTDC Mechanism

Lagrange's equation is utilized to establish the dynamic analysis of the BTDC mechanism [28, 29]. The potential energy, in this case, is ignored since the potential energy for mechanical systems is not a function of velocity or time, while the kinetic energy of the mechanism is derived as follows:

$$T = \frac{1}{2} m_o (\dot{u}_y^4)^2 + \frac{1}{2} m_o (\dot{u}_y^7)^2 + 4 \times \frac{1}{2} m_i (\dot{u}_x)^2 + 8 \times \left[\frac{1}{2} m_f (\dot{u}_x)^2 + \frac{1}{2} \times \frac{1}{12} m_f (\dot{u}_x)^2\right] \tag{34}$$

By taking into consideration half of the stroke length in equation (33) and substituting it in equation (34), the following relationship is obtained:

$$\frac{\partial T}{\partial x} = \frac{{F_a}^2 {R_{amp}}^2}{{K_{tot}}^2} m_o \dot{x} + \frac{2{F_a}^2 {R_{amp}}^2}{{K_{tot}}^2} m_o \dot{x} + 4 m_i \dot{x} + 8 m_f \dot{x} + \frac{2}{3} m_f \dot{x} \tag{35}$$

Given that the mass m_o, m_i and m_f represent output beams mass, input beams mass, and flexure hinges mass, respectively, and by letting $\frac{{F_a}^2 {R_{amp}}^2}{{K_{tot}}^2} = G$ and substituting it in the equation (35), the following is deduced:

$$\frac{d}{dt}\frac{\partial T}{\partial u} = 3 G m_o \ddot{x} + 4 m_i \ddot{x} + \frac{26}{3} m_f \ddot{x} \tag{36}$$

Substitution of Equation (36) is done into the following Lagrange equation, and the free vibration dynamic equation is established as follows:

$$F_x = \frac{d}{dt}\frac{\partial T}{\partial x} - \frac{\partial T}{\partial x} + \frac{\partial V}{\partial x} \tag{37}$$

$$F_x = (3 G m_o + 4 m_i + \frac{26}{3} m_f)\ddot{x} \tag{38}$$

The natural frequency of the BTDC mechanism is then determined as follows:

$$f = \frac{1}{2\pi} \times \sqrt{\frac{K_{tot}}{\left(3 G m_o + 4 m_i + \frac{26}{3} m_f\right)}} \tag{39}$$

2.4. Factors Affecting Stroke and Natural Frequency

Referring to Figure 8's depiction of factors influencing stroke and natural frequency, some parameters positively affect natural frequency while negatively affecting the outcome of a stroke, or contrariwise.

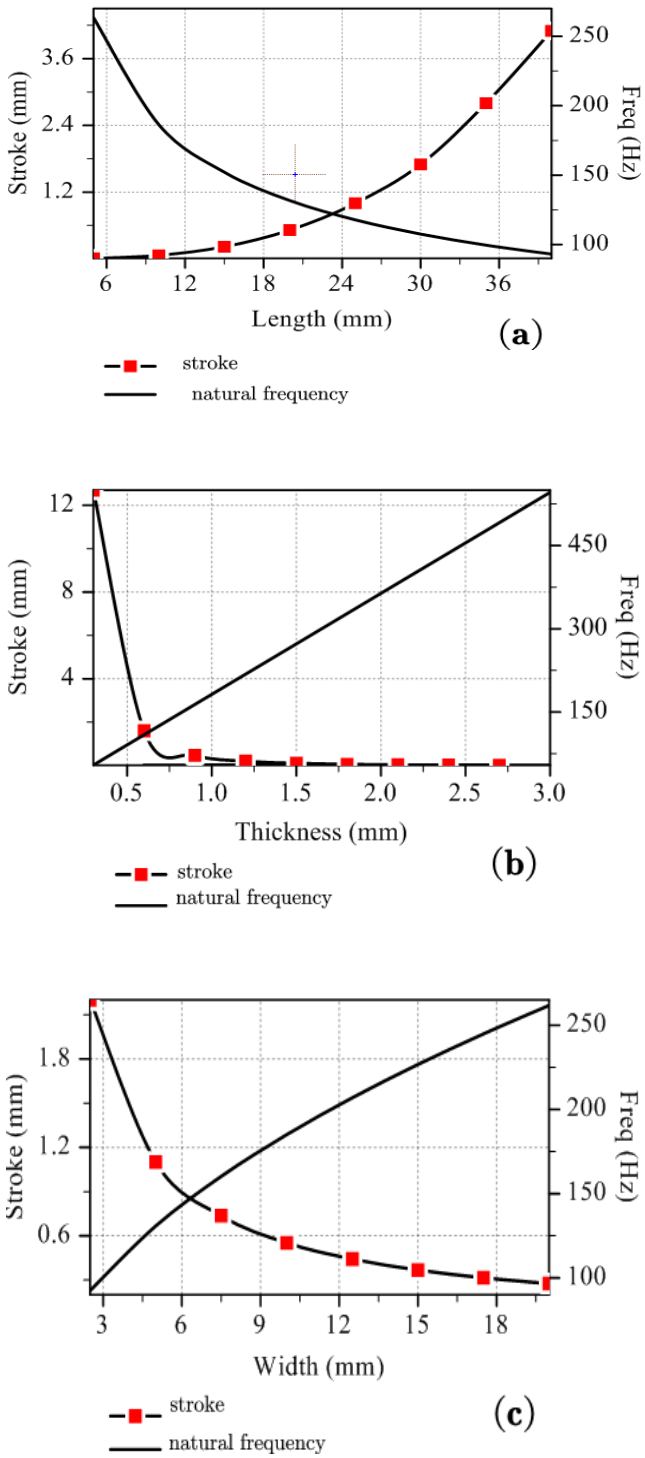

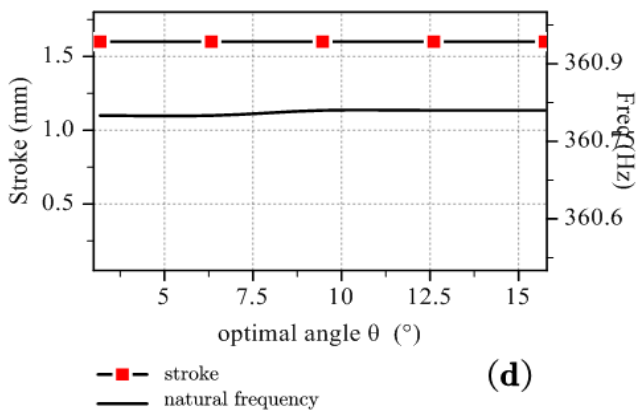

Figure 8. *(a) Length relationship between stroke and natural frequency; (b) Thickness relationship between stroke and natural frequency; (c) Width relationship between stroke and natural frequency; (d) Optimal angles.*

Significant working stroke and an elevated natural frequency are vital for mechanism design, but a compromise between these two parameters is required for an optimum stage design.

2.5. Design Layout and Working Principle of Guiding Mechanism

A few issues must be addressed to maximize stroke when simultaneously analyzing the BTDC mechanism and the NSEA structure. As a result of a very high PM magnetic strength, the BTDC mechanism is susceptible to sticking on stator surfaces, limiting the bridge's desirable mobility. The bridge is vulnerable to tilting since the BTDC mechanism is solely fastened at one end. A guiding mechanism is used to address these emerging issues. Composed of series-connected flexure beams, the guiding mechanism helps to stabilize the bridge by adopting Hooke's law.

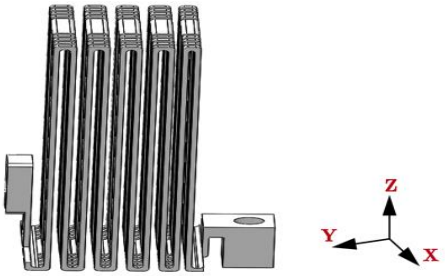

Figure 9. *Guiding mechanism.*

The guiding mechanism depicted in Figure 9 is designed to reduce mobility in the x and z axes directions while facilitating optimal motion along the y-axis path, constituting the stage's total stroke. The guiding mechanism analytical computations are performed by considering its structure and including Hooke's law as follows:

$$F_{gm} = K_{gm} * d \tag{40}$$

The pulling force needed to revert to the point of equilibrium is represented by F_{gm}, the guiding mechanism's motion along the y-axis is shown by d, and the guiding mechanism stiffness is represented by K_{gm}. The guiding mechanism stiffness must not be so elevated to diminish the stage's final motion significantly.

3. Optimal Design of the Nanopositioning Stage

Failure to obtain an appropriate optimization framework limits the commonly utilized usage of nanopositioning stages and results in insufficient functioning of the planned structural design layout. As a result, subject to the effect of numerous constraints, this part develops a coherent optimization framework to improve both mechanical and electromagnetic variables concurrently. Additionally, finite element analysis (FEA) is carried out to confirm the outcomes.

3.1. Optimization of Electromagnetic Parameters

Permanent magnets ($Nd_2Fe_{14}B$) of sizing 10 x 10 x 10mm^3 are utilized featuring Br=1.18T remanence to generate DC bias flux, and a soft material made from DT4 containing a saturation flux density of B_s=1.5T is chosen to manufacture stators and armatures. By considering the desired stroke for motion and defining I_{max} as the largest current that the coil wire is permitted to have, and S_{AF} as the safety factor, the saturation constraint can be written as:

$$NI_{max} \leq \frac{g_0}{\mu_0} * \left[\frac{B_S}{S_{AF}} - \frac{(g_0+|x_{max}|)\alpha_{IF}B_rS_{PM}}{2g_0S_{ST}}\right] \tag{41}$$

The pole surface area of the stator is set as 10 x10 mm^2. Considering the manufacturing tolerances and the desired stroke, the working air gap is set as g_0 = 1mm. From the obtained equation of NI_{max}, the number of turns of coil winding are selected to be $N \leq 105$ and a wire with a 3.5A current maxima is adopted. From equation (12), the actuation force is calculated as $F = 5.92N$.

3.2. Optimization of the BTDC Mechanism

The four corners of the BTDC mechanism are made from DT4, whilst the rest of the structure is forged from aluminum alloy 7075, which has a density of 2770 kg/m^3, Poisson's ratio of 0.3, and Young's modulus of 71000 MPa. The effectiveness of the nanopositioning stage is primarily determined by the structural properties of the compliant mechanism,

which is why they require meticulous alteration. Since the armatures' elastic deformation is much smaller than that of the rest of the structure, only the structural variables linked to the BTDC need to be adjusted, which simplifies the analytical computation. The subsequent optimization framework is developed to optimize the indicator, which is the natural frequency and stroke.

Two objective functions are simultaneously analyzed to attain the intended significant amplification ratio, enhance the natural frequency and maximum stroke that can achieve the desired motion. As a result of the dual directional movement capability of the NSEA within the x-axis generated by the DC flux from the PM, the stroke is twice the movement displacement below the highest actuation force. While modeling the stroke, the negative stiffness of the NSEA must be taken into account. Consequently, the stroke of the stage is as follows:

$$S = \frac{R_{AMP}*n*F}{K_e}\Big|_{max} \geq S_0, \tag{42}$$

Under the maximum current, the maximal actuation force is identified as $F = 5.92N$ from equation (12), n is the number of mechanism sets, and S_0 is the designed stroke. To avoid external disturbance and resonant vibration, the first natural frequency must be retained to attain a high bandwidth [30]. Natural frequency depends on the mass and stiffness of a mechanism; and, to achieve a higher amplification ratio that leads to the required stroke the natural frequency of the structure must not exceed the target natural frequency:

$$f_{max} = \frac{1}{2\pi}\sqrt{\frac{K_{tot}}{\left(3Gm_o+4m_i+\frac{26}{3}m_f\right)}} \leq f_0 \tag{43}$$

The target natural frequency of the mechanism is represented by f_0. By considering factors that influence stroke and natural frequency, the stroke of the mechanism is given first priority as the first objective, followed by natural frequency. The multiobjective function for the optimization framework should then be as follows:

$$f_{o1} = w_1 * \left|\frac{S-S_0}{S_0}\right|,$$

$$f_{o2} = w_2 * \left|\frac{fmax-f_0}{f_0}\right|, \text{ s.t constraints} \tag{44}$$

Respectively, f_{o1} and f_{o2} are the two objective functions mentioned above, f is the in-plane natural frequency and $[w_1, w_2]$ is the weight vector. The considered variables in the optimization process are shown in Table 1. The length of FH affects the stiffness and amplification ratio, contributing to the effective stroke. The thickness of the FH totally contributes to the stiffness in the driven direction. If the thickness of FH is above 2 mm, this drastically reduces the effective stroke of the mechanism; however, if the thickness is below 0.5 mm, it will be difficult to fabricate. The range of the design parameters is validated after considering the mechanism's overall size and manufacturing capacity.

3.3. Design Constraints

3.3.1. Stiffness Constraint

Stiffness is vital in determining the starting frequency of the mechanism, and their inverse relationship, when it comes to achieving a larger displacement, is mitigated by negative stiffness [31]. The negative stiffness efficacy enhances the mechanical efficiency of bridge-type mechanisms, leading to the mechanism's effectiveness [32]. Length, in-plane thickness, and out-of-plane thickness of the mechanism are all factors that affect negative stiffness [33]. Although stiffness directly affects the range of motion and yield stress, preload displacement does not affect stiffness. As a result, the balancing factor may be adjusted to offer various motion ranges, and the resulting equations are employed during the fabrication and testing of the mechanism. The stiffness of a mechanism is vital and an optimal value should be used since a lower value causes harmful effects from external disturbances while a substantial value reduces the ability to attain a higher amplification ratio. The negative stiffness of the armature should be considered to verify the effectiveness of the structure. To get a good balance the equivalent stiffness should be lower than the upper bound of the target stiffness:

$$K_n = \left(\frac{\mu_0 g_0}{2S_{ST}{B_D}^2}\right)^{-1}, \; K_e = K_{in} - K_n \leq K_o \tag{45}$$

K_o and K_{in} are the target stiffness and compliant mechanism stiffness. K_e is the equivalent stiffness of the mechanism by taking into account the negative stiffness K_n characteristic of the NSEA.

3.3.2. Saturation Flux Density Constraint

Saturation magnetic flux density B_s have a direct relation with force and power and the higher it is the higher the force and power generated. However, the driving current should not over-amplify the system hence B_s should not exceed the target saturation magnetic flux density:

$$f(x) = \begin{cases} |B_A + B_{D1}| \\ |B_A - B_{D2}| \end{cases} : f(x) \leq B_s S_{AF} \tag{46}$$

It should be noted that electromagnetic phenomena such as hysteresis and magnetic saturation have complex modeling processes, therefore, the classical linear model Equations (3) and (12) are employed to reduce the model complexity [4].

3.3.3. Stress Constraint

Stress evaluation prevents material from experiencing the maximum stress that would otherwise cause plastic failure [3]. The deformation of the FH should be elastic throughout the

actuation procedure; therefore, the thinnest part of the FH experiences maximal stress σ_{max} when input displacement reaches the maximum value. To provide a dependable linear motion resulting from the elastic deformation of FHs, the maximal stress created inside the model must always remain below the material's maximum stress permitted. The maximum mechanical stress constraint is described as:

$$\sigma_{max} = \frac{S_0 1.5Et}{L^2}\sigma_s \leq |\sigma| = \frac{\sigma_m}{S_{AF}} \quad (47)$$

The stress concentration factor is represented by σ_s and $|\sigma|$ is the maximum allowable stress; σ_m is the yield stress of the FH's material and S_{AF} is the safety factor.

3.4. Optimization of the Guiding Mechanism

The guiding mechanism must be tuned in order to provide the best possible end motion. The trial-and-error technique is used to optimize the thickness, length, and height of the double flexure beams seen in Figure 10.

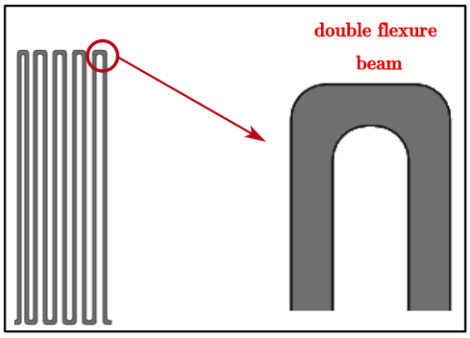

Figure 10. *Guiding mechanism left side view inner section.*

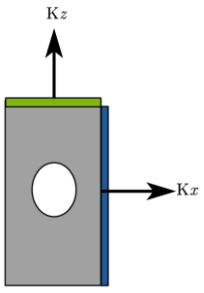

Figure 11. *Guiding mechanism output section.*

During optimization of the GM, lateral stiffness is of great importance. The lateral stiffness K_z of the guiding mechanism in Figure 11 should not be greater than the stiffness along the x-axis represented by K_x; in addition, K_x stiffness at the output node when there is no guiding mechanism should be less than the K_x stiffness of the guiding mechanism. When these objectives are satisfied the guiding mechanism will not drastically affect the overall stroke.

3.5. Optimization Results

The ANSYS Maxwell 2D module is employed to produce a DC field plot that shows flux lines with respect to the necessary structural variables, which is then adopted to calculate the leakage factor α_{IF} used for the NSEA. After assigning the materials, the PMs magnetic direction is changed to point in the desired direction. The PMs have remanence B_r= 1.18T and magnetic coercivity H_c = -868000 A/m specified as their attributes. The material's relative permeability is chosen to be nonlinear, and a B-H curve is used. DT4 is attributed to stators and armatures. The boundary is allocated to indicate the extension of the magnetic field. The solution configuration is then applied, examined, and the outcome displayed in Figure 12 is observed under the fields in the B-vector. Equation (6) can be utilized to determine the flux from the PM entering the armature Φ and the total flux exiting the PM Φ_T by noting the number of flux lines on the derived plot seen in Figure 12.

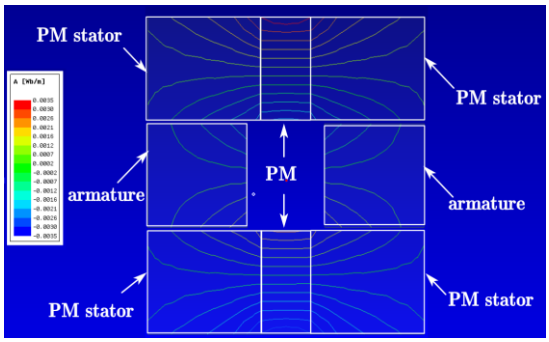

Figure 12. *Derived flux lines plot.*

Given the underlying premise that R_{PM} is regarded as infinity, and taking into account Equation (6), the result finding stated above clearly shows that the above approach approximates the ratioϕ/ϕ_T. As a result, the ratio of $\phi/\phi_T$from FEA may be used to determine the leakage factor for similar models. These computations show that the biasing flux B_{D1} and B_{D2} are actually linear functions of x, while the previously indicated parameters Φ and B_D are variables that do not depend on x.

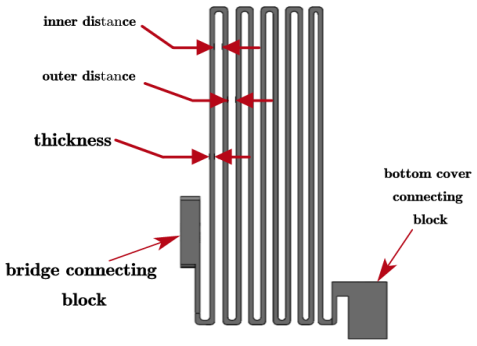

Figure 13. *Guiding mechanism's left side view.*

The guiding properties in Table 1, further illustrated in Figures 13 and 14, are utilized to design the guiding mechanism.

Table 1. *Guiding mechanism properties.*

Quantity	Details
Design	Utilizes five double flexure beams with fillet angles of R0.5mm
Inner thickness (Left Side View)	[0.6, 1.1] mm range; 3 inner beams are 1.0mm; exterior beam is 0.6mm.
Outer distance (Left Side View)	[0.6, 1.1] mm range; matching inner thickness directions.
Bridge connecting block	Dimensions: 9 x 2.5 x 4.79mm^3
Bottom cover connecting block	Dimensions: 8 x 5 x 6mm^3
Top view structure	1 double flexure beam (9 sections): central beam (6,5mm) + 4 small beams (0,75mm each) on each side, separated by 0.75mm.
Total model height	44.6 mm

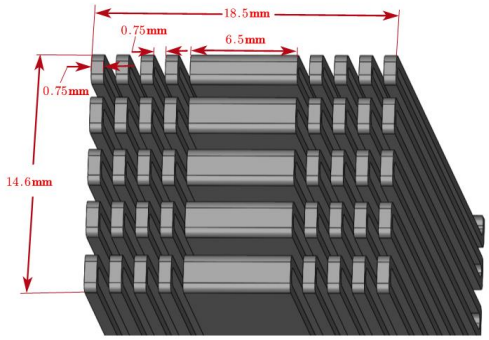

Figure 14. *Top view of Guiding mechanism.*

The optimization process includes the use of the genetic algorithm [34]. The ideal outcome is obtained using MATLAB's Multiobjective Optimization via Genetic Algorithm solver (gamultiobj). The compactness of the structure largely determined the final solutions; additionally, the variables and the solver's Pareto optimal frontier contributed to the finalized solutions' performance-based determination. The distribution pattern resulting from the Pareto points during selection shows how the system's goals are traded off. The target of the chosen amplification ratio, natural frequency, and stroke is promptly achieved once the optimization effectively converges. The finite element analysis (FEA) simulation and manufacturing procedure then make use of the set of approximation values.

Table 2. *Multiobjective optimization solutions using GA solver.*

Quantity	Symbol	Constraint range	Optimal result
Length of FH	L (mm)	$[1, 30]$	28.999mm
Thickness of FH	t (mm)	$[0.5, 2.5]$	0.601 mm
Width of FH	b (mm)	$[0, 10]$	3.492 mm
The angle between FH and armature	θ (°)	$[1°,\ 15°]$	3.1813°

A genetic algorithm [34] is incorporated into the optimization procedure. Multiobjective optimization using a genetic algorithm solver (gamultiobj) in MATLAB is used to derive the optimal results, as illustrated in Table 2. The compactness of the structure played a key factor in determining the final solutions; in addition, Pareto's optimal frontier from the solver and the variables helped determine the final solutions depending on the performance. The tradeoff between the objectives of the structure is illustrated in the distributing trend of the Pareto points for selection. After the optimization efficiently converges, the goal of the designated amplification ratio, natural frequency, and stroke is quickly realized. The

approximation values are then utilized in the FEA simulation and fabrication.

3.6. Finite Element Based Numerical Verification

Finite element verification of the electromagnetic and mechanical properties is done to authenticate the analytically optimized structure using the ANSYS Maxwell and Workbench modulus, respectively.

3.6.1. Electromagnetic Simulation

The electromagnetic flux density distribution, which results in the EM circuit shown in Figure 15, accounts for the combined influence of the PM and coil wire with a maximum current of 3.5A. The magnetic circuit's 3D magnetic flux density is estimated using the length-based mesh generation process and the inclusion of DT4's B-H curve. Primarily, the air gap flux distribution along the x-direction is examined because the flux density in that direction assists in the formation of the actuation force. The estimated average flux density within the air gaps ranges from 0.211T to 0.471T, as shown in Table 3; the flux bias resulting from the PM is responsible for the density discrepancy. The maximum magnetic flux density is 1.484 T (< B_S= 1.5 T), which is below the saturation flux density point 1.5, suggesting that the required force is generated before reaching a point beyond which magnetic flux density inside the structure material cannot increase with an increase of MMF (NI). When the mathematical force is combined, the maximal actuation force calculated by FEA is approximately F_x= 5.45 N, which deviates only 8.48% from the 5.92 N theoretical force.

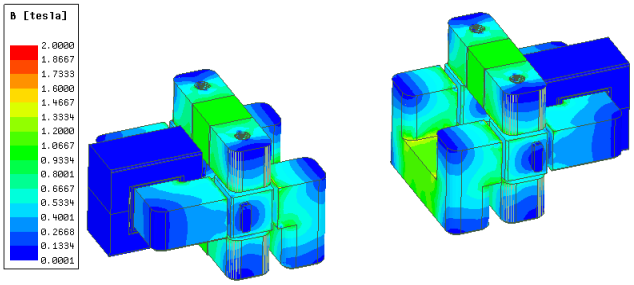

Figure 15. *Flux distribution electromagnetic simulation result.*

Table 3. *Deviation between Analytical and FEA Electromagnetic models*

	Analytical model	FEA model	Deviation
F_x	5.92 N	5.45 N	8.45 %
B_S	Saturation flux density	1.5 T	1.07 &
	Maximum B of mechanism	1.484 T	

3.6.2. Mechanical Simulation

FEA simulation is necessary to verify that the analytical model presented previously is accurate. In ANSYS Workbench, the finite model is imported from SOLIDWORKS, and the material assignment is done together with mesh generation. In Static structure, the bottom body of the bridge is fixed, followed by force assignment on all four armatures, thereby achieving the required mechanism displacement constraints. The deviation between the analytical and FEA model results of the mechanism is illustrated in Table 4. The FEA total deformation simulation is shown in Figure 16(a). The maximum stress is simulated by equally distributing the maximum driving force towards the actuators, and its value is obtained as 12.85 MPa, as shown in Figure 16(b). The physical structure is immune to fatigue failure since the obtained maximum stress is below the aluminum alloy's 250 MPa yield strength.

Table 4. *Deviation between Analytical and FEA Mechanical models*

	RAMP	KIN	Frequency	Stroke
Analytical	29.68	1.10N/μm	355Hz	0.159mm
FEM	29.93	1.15N/μm	360.75Hz	0.154mm
Deviation	0.84 %	4.35 %	1.59 %	3.25 %

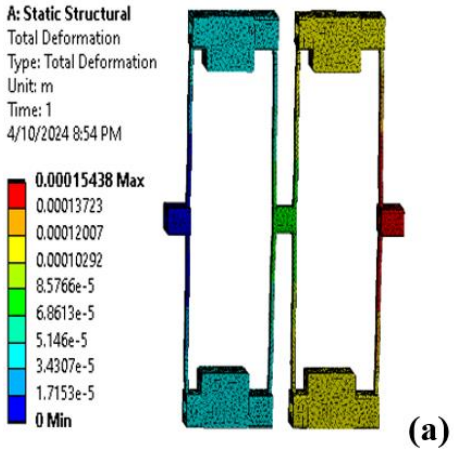

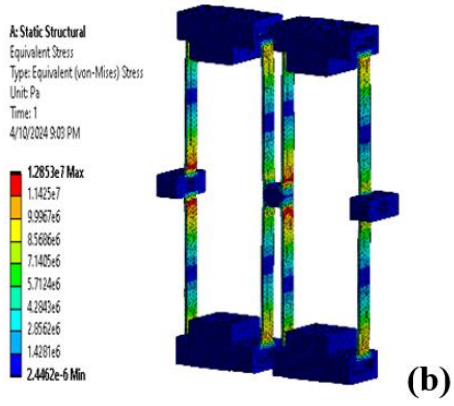

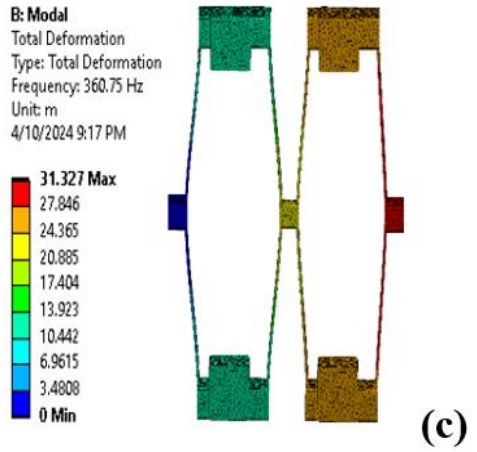

Figure 16. *(a) Total deformation of BTDC; (b) Equivalent stress; (c) Mode 1 natural frequency.*

A modal study of the bridge is done to examine the dynamic behavior of the BTDC mechanism. Six modal shapes were analyzed, and Figure 16(c) shows the first mode that corresponds with the desired motion and illustrates the lowest deformation at which deformation occurs. The six resonant frequencies are observed from 360.75 Hz to 780.82 Hz. This study will prioritize the first mode since it specifies the maximum loads in a mechanism and how the vibrating structure will relate to the surrounding systems.

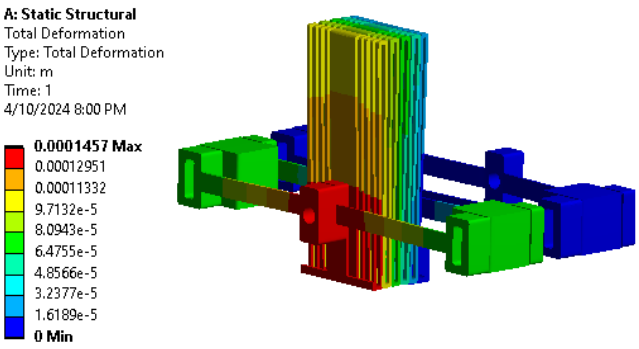

Figure 17. *Guiding mechanism's total deformation.*

Figure 17 illustrates the overall deformation that occurs when the guiding mechanism is used. Table 5 displays the effects of the guiding mechanism on the final stroke of the entire mechanism. Using a guiding mechanism increases stiffness along the y-axis direction, which reduces the amplification ratio by approximately 2.37%. Due to the significant 99.5% reduction in displacement along the z-axis direction Δz, the bridge mechanism will fail to stick along the z-axis direction.

Table 5. *Effects of guiding mechanism (GM).*

	Stroke	**Ramp**	Δz	K_x	K_y
No GM	0.15mm	29.93	0.237mm	273.7N/μm	0.00212N/μm
GM	0.139mm	29.22	0.0013mm	443.7N/μm	0.00242N/μm
Deviation %	9.7%	2.4%	99.5%	62.1 %	14.2 %

This implies that when the guiding mechanism is used, the stiffness K_z rises noticeably. The stroke and amplification ratio of the stage are only marginally affected by the guiding mechanism, which only raises the stiffness along the direction of the final stroke by 14.2%.

4. Experimental Testing

4.1. Experiment Setup

The complete layout of the nanopositioning stage, measuring roughly 124 ×58 ×50 mm3, is depicted in Figure 18. It consists primarily of the NSEA and the BTDC mechanism, which work jointly to generate the motion of the whole travel range. This graphic amply illustrates the prototype's exceptional compactness. A MicroSense Corporation capacitive displacement sensor with a 20 KHz bandwidth and a board 38470 with probe T22725, that provides a measurement range of ±250 μm, is used to quantify the precise displacement inside the y-axis.

The prototype's output end is extremely near to where the sensor probe is fixed. In order to obtain optimal readings, the reading of the sensor is calibrated to zero before conducting the experiment after turning on the Microsense board. The data acquisition board receives the signal from the Microsense board. This reading is shown on the power amplifier, which has a power line that supplies a voltage of roughly 24 V. The prototype's coil windings are carefully linked to both the negative and positive ports of the insulated negative and positive wires from the power amplifier. A brown wire represents the positive wire, while the negative wire is represented by a blue wire. A straightforward linear servo amplifier (SMA5005-1, GLENTECH Company) with a gain of 0.8A/V is utilized to improve the control command in order to excite the excitation windings. The prototype will start moving when it receives a stimulation signal coming from the

power amplifier. When testing motion, a single Hertz frequency is employed because using higher frequencies may cause the output end to vibrate rapidly, disrupting the prototype. Furthermore, as stroke is the mechanism's static feature, testing simply uses a tiny frequency.

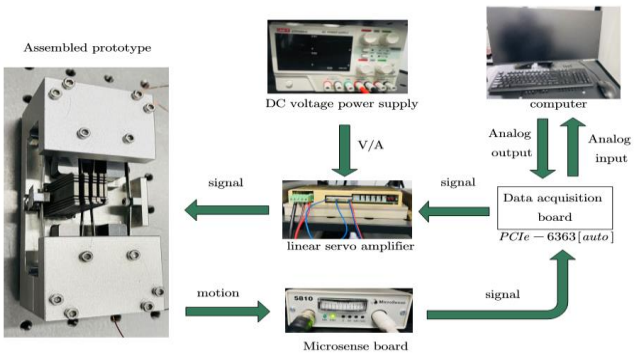

Figure 18. *Overall experimental procedure flowchart.*

4.2. Results and Discussion

The motion range is analyzed using a sinusoidal command with a low frequency of roughly one Hertz and a maximum allowable amplitude of precisely 4.375V/ 3.5A, as displayed in Figure 19. The overall displacement of the stage was about 52µm, and a noticeable hysteresis loop was observed in Figure 20, peaking at about 18.7µm. The stage's positive direction motion accounted for approximately 35.9% of the total motion span, resulting in nearly three times the negative direction motion.

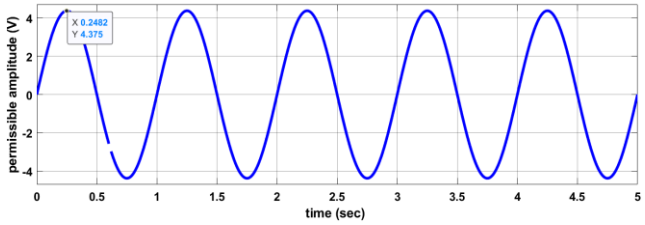

Figure 19. *Input signal using 3.5A / 4.375V*

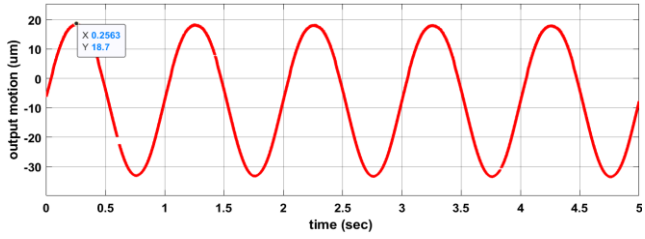

Figure 20. *Output motion at 3.5A (4.375V)*

The prototype's output motion rises in proportion to the strength of the actuation signal applied to it. A sweep excitation is used to obtain the frequency response characteristic. This is accomplished by using a harmonic command with a fixed amplitude of precisely 0.1875 V and a continually varying frequency ranging from 0.01 Hz to 500 Hz at a target time of one second as shown in Figure 21. As demonstrated in Figure 22, the resultant frequency response function is created by performing Fourier transformation on both the input command and the subsequent output response. The resulting response function is considered to represent the practical frequency response function.

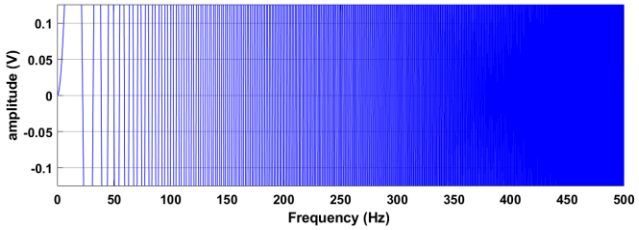

Figure 21. *Input sweep signal*

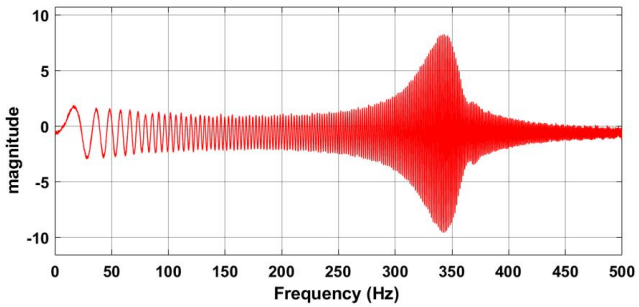

Figure 22. *Sweep signal output.*

Its primary dynamics are seen as a third-order system that determines the estimated frequency response function. By identifying s as a Laplace function and determining the amplitude, phase lag, and resonant frequency, a continuous time transfer function is expressed as follows:

$$G_D(s) = \frac{(8.688*10^{-8})}{s^3+260.8s^2+(4.39*10^6)s+(8.688*10^{-8})} \quad (48)$$

The comparison of the practical frequency response function in Figure 23 and the estimated frequency response function displayed in Figure 24 suggests a good agreement, implying that the estimated model $G_D(s)$ is reliable for the prototype's control system design that follows. At remarkably low frequencies, the gain in the practical function plot commences at 13.97 dB and then starts to drop at about 10 Hz (13.56 dB). The gain displayed in the estimated function plot begins at about 0 dB and progressively decreases, starting at 10 Hz (-0.38 dB). The estimated plot's progressive decline in the 10 – 195 Hz range is approximately 11.8 dB, but the practical plot's progressive decline is

approximately 4.27dB. As a result, the practical drop is 36.2% of the estimated drop. Thereafter, there is a sharp rise to the highest frequency of about 333 Hz in both figures. The only differences between these two plots of frequency response functions are in the amplitude, size, and phase angle.

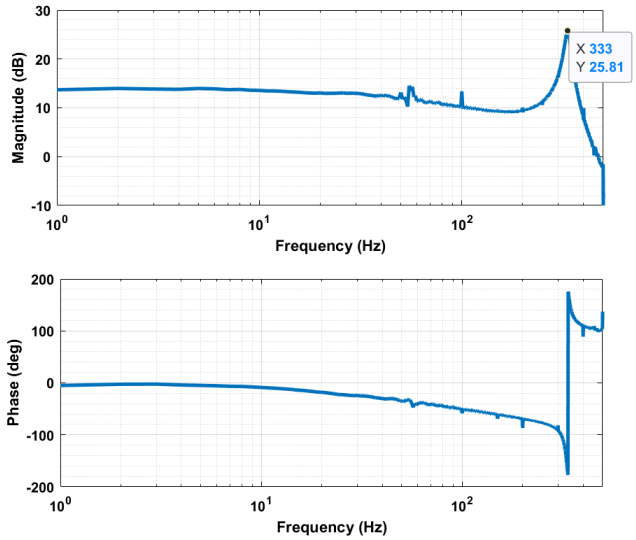

Figure 23. *Practical frequency response*

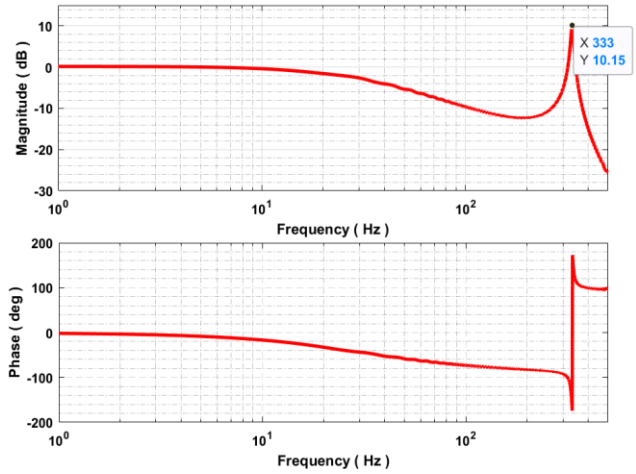

Figure 24. *Estimated from transfer function*

The practical frequency response function's resonant peak, which is 333 Hz—6.177% higher than the analytical value of 355 Hz—is the source of the natural frequency's first mode. This results from the drop in stiffness caused by manufacturing error.

4.3. Control System Design

The block diagram of the employed control system is illustrated in Figure 25. The prototype's actuation axis is viewed as a single-input, single-output (SISO) system for feedback control purposes. Any system nonlinearities are effectively gathered together as perturbations that the feedback mechanism must balance out. In the continuous time domain, a proportional-integral-derivative (PID) controller is used in parallel form. By letting C_p represent the proportional gain that handles the error signal, C_i as the integral gain that controls the error from previous time to present time, C_d as the derivative gain that controls the derivative of error and N as the filter coefficient, the following formula is expressed:

$$G_P(s) = C_p\left(1 + \frac{C_i}{C_p s} + \frac{C_d N s}{C_p(N+s)}\right) \tag{49}$$

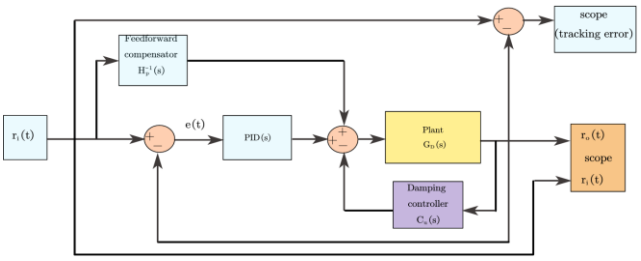

Figure 25. *Control system block diagram*

Using an empirical approach based on testing, all the appropriate PID controller parameter settings are entered. These parameters fully modify the plant to get the desired result. During initialization, the integrator and filter's initial conditions are set to zero, and zero crossing detection gets activated.

The closed-loop control system's output is assessed and compared to the desired set point, while the PID controller serves as the primary system controller. Then, utilizing the error signal to modify the system's control input, a feedback loop is established. On the other hand, errors could result from outside disruptions that affect the system's output. This control system incorporates a feedforward compensator $H_p^{-1}(s)$ Improve system performance by anticipating and reducing the effect of external disturbances on output. The feedforward compensator will lessen the effect of these external disturbances by using the system model and the detected disturbance to identify the necessary control input to adjust for the disturbance before it affects the system's output. This can reduce the error caused by outside variables and enhance the control system's accuracy, stability, and responsiveness. $H_P(s)$ is lowered to a constant gain to avoid inverting the high-order system, which must be corrected. In order to achieve high accuracy control, an enhanced gain external loop controller will be employed by reducing system resonances by the incorporation of a second-order damping controller, $C_u(s)$. It is suggested that the system is underdamped. With ξ acting as the system's damping ratio and the undamped natural frequency $\omega_n = \frac{\omega_d}{\sqrt{1-\xi^2}}$, the damping controller $C_u(s)$ is adopted as follows:

$$C_u(s) = \frac{{\omega_d}^2}{(s-\xi^2 s)\left(s^2+\frac{2\xi\omega_d s}{\sqrt{1-\xi^2}}+\frac{{\omega_d}^2}{1-\xi^2}\right)} \quad (50)$$

The appropriate damping behavior is attained once all adjustable parameters have been tuned.

4.4. Tracking Control Performance

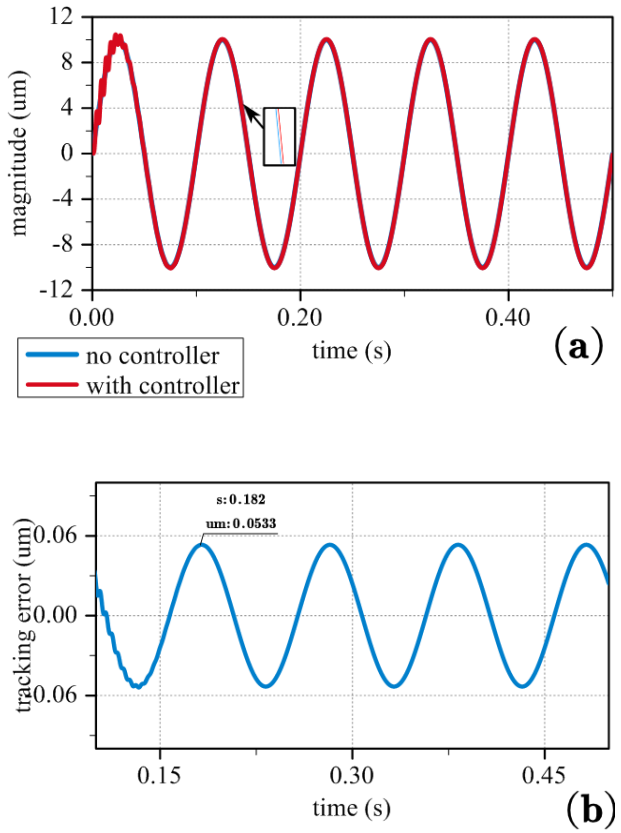

Figure 26. *(a) Tracking outcome of the system; (b) Tracking error.*

In order to examine the entire system's control performance, Figure 26(a) displays the tracking result performance, and Figure 26(b) shows the tracking error over time. The highest tracking error, considering a motion range of ly 10 μm, is $\pm 0.0533\ \mu m$, which means that it is 0.53% of the 10 μm motion.

5. Conclusion

In conclusion, this research addressed the need for a long-range motion-compliant nanopositioning stage driven by an NSEA. The objective was to design, model, optimize, and experimentally evaluate a high-precision nanopositioning stage capable of accurate positioning over extended distances. Integrating the NSEA and BTDC mechanisms effectively achieved greater stroke and enabled long-range motion. The variables affecting natural frequency and stroke were also expressed, and design constraints were analyzed. The mathematical model results were validated using the FEA simulation. A prototype nanopositioning stage was successfully developed through comprehensive analysis and optimization, exhibiting high precision and accuracy. Experimental tests were divided into open-loop and closed-loop tests. For the open loop test during motion testing, a 3.5A input signal was utilized to attain a 52um final motion. A sweep signal was used to determine the natural frequency, and the frequency response function reached its peak at 333 Hz, which is 6.197% lower than the analytical frequency of 355 Hz. During the closed-loop experimental test, the control system was constructed to produce a closed-loop system. Additionally, the system's control performance was examined, and it was discovered that the tracking error for a 10 um motion was only 0.53%, indicating that the model is good. The experimental tests, including motion and natural frequency tests, validated the prototype's performance, and the closed loop test demonstrated its feasibility for practical engineering applications. Future research should explore further improvements in control systems to enhance precision and response times. Additionally, investigating alternative materials could enhance the performance and durability of nanopositioning stages.

Abbreviations

NSEA	Normal Stressed Electromagnetic Actuator
BTDC	Bridge Type Distributed Compliant Mechanism
FH	Flexure Hinge
GM	Guiding Mechanism
FEA	Finite Element Analysis
SISO	Single-Input Single-Output
PID	Proportional-Integral-Derivative

Acknowledgments

The authors extend their gratitude to Zhiwei Zhu (Full Professor at the School of Mechanical Engineering at Nanjing University of Science and Technology) for this supervision during this study.

Author Contributions

Chido Celine Chogugudza: Conceptualization, Methodology, Formal Analysis, Data curation, Validation, Visualization, Writing – original draft, Writing – review & editing

Yan-Ning Fang: Methodology, Resources, Software, Project administration

Zi-Hui Zhu: Investigation, Software, Funding acquisition, supervision

Funding

This work is supported by the Outstanding Youth Founda-

tion of Jiangsu Province of China (BK 20211572) and the Fundamental Research Funds for the Central Universities (30921013102).

Data Availability Statement

The data is available from the corresponding author upon reasonable request.

Conflicts of Interest

The authors declare no conflicts of interest.

References

[1] A. Yacoot *et al.*, "Design and performance of a test rig for evaluation of nanopositioning stages," vol. 30, no. 3, p. 035002, 2019. https://doi.org/10.1088/1361-6501/aafd03

[2] S. Iqbal, A. J. S. Malik, and A. A. Physical, "A review on MEMS-based micro displacement amplification mechanisms," vol. 300, p. 111666, 2019. https://doi.org/10.1016/j.sna.2019.111666

[3] Q. Xu, Y. J. M. Li, and m. theory, "Analytical modeling, optimization and testing of a compound bridge-type compliant displacement amplifier," vol. 46, no. 2, pp. 183-200, 2011. https://doi.org/10.1016/j.mechmachtheory.2010.09.007

[4] W.-W. Huang, L. Li, Z. Zhu, L.-M. J. M. S. Zhu, and S. Processing, "Modeling, design and control of normal-stressed electromagnetic actuated fast tool servos," vol. 178, p. 109304, 2022. https://doi.org/10.1016/j.ymssp.2022.109304

[5] L.-J. Lai and X.-Q. Yin, "Analysis of Bridge-type Distributed-compliance Mechanism," in *MATEC Web of Conferences*, 2018, vol. 213, p. 01005: EDP Sciences. https://doi.org/10.1051/matecconf/201821301005

[6] W.-L. Zhu *et al.*, "Design, modeling, analysis and testing of a novel piezo-actuated XY compliant mechanism for large workspace nanopositioning," vol. 25, no. 11, p. 115033, 2016. https://doi.org/10.1088/0964-1726/25/11/115033

[7] D. Wu, X. Xie, and S. J. I. T. o. M. Zhou, "Design of a normal stress electromagnetic fast linear actuator," vol. 46, no. 4, pp. 1007-1014, 2009. https://doi.org/10.1109/TMAG.2009.2036606

[8] Z. Zhou, Y. Gao, L. Sun, W. Dong, and Z. J. M. S. Du, "A bistable mechanism with linear negative stiffness and large in-plane lateral stiffness: design, modeling<? xmltex\break?> and case studies," vol. 11, no. 1, pp. 75-89, 2020. https://doi.org/10.5194/ms-11-75-2020, 2020.

[9] M. Ling, J. Cao, M. Zeng, J. Lin, D. J. J. S. M. Inman, and Structures, "Enhanced mathematical modeling of the displacement amplification ratio for piezoelectric compliant mechanisms," vol. 25, no. 7, p. 075022, 2016. https://doi.org/10.1088/0964-1726/25/7/075022

[10] J.-L. Ha, Y.-S. Kung, S.-C. Hu, R.-F. J. S. Fung, and A. A. Physical, "Optimal design of a micro-positioning Scott-Russell mechanism by Taguchi method," vol. 125, no. 2, pp. 565-572, 2006. https://doi.org/10.1016/j.sna.2005.06.025

[11] G. Haertling, "Compositional study of PLZT Rainbow ceramics for piezo actuators," in *Proceedings of 1994 IEEE International Symposium on Applications of Ferroelectrics*, 1994, pp. 313-318: IEEE. https://doi.org/10.1109/ISAF.1994.522366

[12] J. Ueda, T. W. Secord, and H. H. J. I. A. t. o. m. Asada, "Large effective-strain piezoelectric actuators using nested cellular architecture with exponential strain amplification mechanisms," vol. 15, no. 5, pp. 770-782, 2009. https://doi.org/10.1109/TMECH.2009.2034973

[13] C. Lin, Z. Shen, Z. Wu, J. J. S. Yu, and A. A. Physical, "Kinematic characteristic analysis of a micro-/nano positioning stage based on bridge-type amplifier," vol. 271, pp. 230-242, 2018. https://doi.org/10.1016/j.sna.2017.12.030

[14] M. Ling, J. Wang, M. Wu, L. Cao, B. J. S. Fu, and A. A. Physical, "Design and modeling of an improved bridge-type compliant mechanism with its application for hydraulic piezo-valves," vol. 324, p. 112687, 2021. https://doi.org/10.1016/j.sna.2021.112687

[15] S. Polit and J. J. I. A. T. o. m. Dong, "Development of a high-bandwidth XY nanopositioning stage for high-rate micro-/nanomanufacturing," vol. 16, no. 4, pp. 724-733, 2010. https://doi.org/10.1109/TMECH.2010.2052107

[16] P. Huang, X. Wu, S. To, L. Zhu, Z. J. I. J. o. M. T. Zhu, and Manufacture, "Deterioration of form accuracy induced by servo dynamics errors and real-time compensation for slow tool servo diamond turning of complex-shaped optics," vol. 154, p. 103556, 2020. https://doi.org/10.1016/j.ijmachtools.2020.103556

[17] S. Jin and X. Wang, "Rotating Electromagnetic Actuator with Magnetic Fluid," in *Journal of Physics: Conference Series*, 2022, vol. 2183, no. 1, p. 012006: IOP Publishing. https://doi.org/10.1088/1742-6596/2183/1/012006

[18] L. Chen *et al.*, "A novel compliant nanopositioning stage driven by a normal-stressed electromagnetic actuator," vol. 19, no. 4, pp. 3039-3048, 2021. https://doi.org/10.1109/TASE.2021.3105683

[19] N. Lobontiu, E. J. C. Garcia, and structures, "Analytical model of displacement amplification and stiffness optimization for a class of flexure-based compliant mechanisms," vol. 81, no. 32, pp. 2797-2810, 2003. https://doi.org/10.1016/j.compstruc.2003.07.003

[20] P. Liu, P. J. M. Yan, and M. Theory, "A new model analysis approach for bridge-type amplifiers supporting nano-stage design," vol. 99, pp. 176-188, 2016. https://doi.org/10.1016/j.mechmachtheory.2016.01.005

[21] J. Kim and J. J. I. T. o. M. Chang, "A new electromagnetic linear actuator for quick latching," vol. 43, no. 4, pp. 1849-1852, 2007. https://doi.org/10.1109/TMAG.2006.892289

[22] Q. Zhang, J. Zhao, X. Shen, Q. Xiao, J. Huang, and Y. J. M. Wang, "Design, modeling, and testing of a novel xy piezo-actuated compliant micro-positioning stage," vol. 10, no. 9, p. 581, 2019. https://doi.org/10.3390/mi10090581

[23] H.-W. Ma, S.-M. Yao, L.-Q. Wang, Z. J. S. Zhong, and A. A. Physical, "Analysis of the displacement amplification ratio of bridge-type flexure hinge," vol. 132, no. 2, pp. 730-736, 2006. https://doi.org/10.1016/j.sna.2005.12.028

[24] W. Huang, J. Lian, M. Chen, and D. J. M. An, "Bidirectional active piezoelectric actuator based on optimized bridge-type amplifier," vol. 12, no. 9, p. 1013, 2021. https://doi.org/10.3390/mi12091013

[25] J. H. Kim, S. H. Kim, Y. K. J. S. Kwak, and A. A. Physical, "Development and optimization of 3-D bridge-type hinge mechanisms," vol. 116, no. 3, pp. 530-538, 2004. https://doi.org/10.1016/j.sna.2004.05.027

[26] Y. Koseki, T. Tanikawa, N. Koyachi, and T. J. A. R. Arai, "Kinematic analysis of a translational 3-dof micro-parallel mechanism using the matrix method," vol. 16, no. 3, pp. 251-264, 2002. https://doi.org/10.1163/156855302760121927

[27] K.-q. Qi, Y. Xiang, C. Fang, Y. Zhang, C.-s. J. M. Yu, and M. Theory, "Analysis of the displacement amplification ratio of bridge-type mechanism," vol. 87, pp. 45-56, 2015. https://doi.org/10.1016/j.mechmachtheory.2014.12.013

[28] S. Xiao and Y. J. I. T. o. I. E. Li, "Optimal Design, Fabrication, and Control of an $ XY $ Micropositioning Stage Driven by Electromagnetic Actuators," vol. 60, no. 10, pp. 4613-4626, 2012. https://doi.org/10.1109/TIE.2012.2209613

[29] X. Wang *et al.*, "Design, modeling, and test of a normal-stressed electromagnetic actuated compliant nanopositioning stage," vol. 185, p. 109753, 2023. https://doi.org/10.1016/j.ymssp.2022.109753

[30] B. Ding, Z.-X. Yang, G. Zhang, and X. J. A. i. M. E. Xiao, "Optimum design and analysis of flexure-based mechanism for non-circular diamond turning operation," vol. 9, no. 12, p. 1687814017743353, 2017. https://doi.org/10.1177/1687814017743353

[31] X. Huang, X. Liu, J. Sun, Z. Zhang, H. J. J. o. S. Hua, and vibration, "Vibration isolation characteristics of a nonlinear isolator using Euler buckled beam as negative stiffness corrector: a theoretical and experimental study," vol. 333, no. 4, pp. 1132-1148, 2014. https://doi.org/10.1016/j.jsv.2013.10.026

[32] W. Dong *et al.*, "Development of a highly efficient bridge-type mechanism based on negative stiffness," vol. 26, no. 9, p. 095053, 2017. https://doi.org/10.1088/1361-665X/aa8102

[33] K. Hoetmer, G. Woo, C. Kim, and J. Herder, "Negative stiffness building blocks for statically balanced compliant mechanisms: design and testing," 2010. https://doi.org/10.1115/1.4002247

[34] D. Corne and M. A. Lones, "Evolutionary algorithms," in *Handbook of Heuristics*: Springer, 2018, pp. 409-430. https://doi.org/10.1007/978-3-319-07153-4_27-1

Biography

Chido Celine Chogugudza is a postgraduate student at Nanjing University of Science and Technology, Mechanical Engineering Department. She received her BE in Mechanical Design, Manufacturing, and Automation from Jiangsu University of Science and Technology, Zhenjiang, China, in 2021. Currently pursuing her Master of Mechanical Engineering, her research interest is ultra-precision manufacturing technology and automation.

Yan-Ning Fang received the BE degree in mechanical engineering and automation from Shandong University of Science and Technology, Shandong, China, in 2019. He is working towards his PhD at the School of Mechanical Engineering, Nanjing University of Science and Technology, Nanjing, China. His research interests include designing, optimizing, and controlling electromagnetically driven nanopositioning systems.

Zi-Hui Zhu received a BE degree in process equipment and control engineering from Yangtze University, Jingzhou, China 2017. He is working toward a Ph. D. with the Nanjing University of Science and Technology, Nanjing, China. His research interests include the ultra-precision finishing of complex optics.

Research Field

Chido Celine Chogugudza: Machine Design, Electromagnetic Field Modeling, Automation, Ultra-precision Manufacturing Technology, Control of Nanopositioning stages, Optimization of Displacement Amplifiers.

Yan-Ning Fang: Electromagnetic Field Modeling, Optimization of Electromagnetic Micro-nano Drive, Magnetic Levitation Plane Motor, Precision Motion Control of Motor, Ultra-precision Machining of Optical Components.

Zi-Hui Zhu: Machine Design, Electromagnetic Field Modeling, Ultra-precision Manufacturing Technology, Precision Motion Control, Micro-polishing, Automation.